plasma

MDPI

Article

Underwater Electrical Explosions of Different Metal Wires on the Microsecond Timescale

Ron Grikshtas *, Sergey Efimov, Nikita Asmedianov and Yakov E. Krasik

Physics Department, Technion—Israeli Institute of Technology, Haifa 3200003, Israel; fnkrasik@physics.technion.ac.il (Y.E.K.)
* Correspondence: ron.gri@campus.technion.ac.il

Abstract

Underwater electrical explosions of single metallic wires driven by microsecond current pulses are investigated and compared with previously reported sub-microsecond experiments. Current and voltage waveforms, streak camera shadow imaging, and one-dimensional hydrodynamic simulations are employed to characterize how the energy density, energy density deposition rate, and the generated shock waves in water depend on the wire parameters. It was found that, similar to the sub-microsecond timescale, the solid–liquid phase transition occurs later than thermodynamic calculations predicted, while the liquid–vapor phase transition happens sooner than expected, leading to a two-phase coexistence. Additionally, most materials show a notable resistance peak (Ti, Fe, Ni, Zn, Ag, Sn, Ta, Au) compared to a quasi-plateau for Cu and Mo or a continuous increase for Al and Pt. Moreover, the specific action integral values are significantly smaller than those observed in wire explosion experiments in vacuum. Finally, the plasma formed at peak resistive voltage is non-ideal but exhibits lower electron density, ionization degree, and temperature compared to the sub-microsecond case.

Keywords: exploding wire method; phase transitions; electrical properties and parameters; pulse generators; equations of state; high energy density physics; shock waves; hydrodynamics simulations

Check for updates

Academic Editor: Andrey Starikovskiy

Received: 13 December 2025
Revised: 23 January 2026
Accepted: 8 February 2026
Published: 11 February 2026

Copyright: © 2026 by the authors. Licensee MDPI, Basel, Switzerland. This article is an open access article distributed under the terms and conditions of the Creative Commons Attribution (CC BY) license.

1. Introduction

Electrical wire explosions (EWEs) provide a versatile platform for investigating warm dense matter, a central topic in high-energy-density physics [1–3]. EWEs involve rapid Joule heating of a wire under strong self-magnetic fields (>10 T), leading to successive solid–liquid–vapor–plasma transitions [4–7]. EWEs are accompanied by magnetohydrodynamic (MHD) and overheating (electrothermal) instabilities [8–12], and shock wave generation [13–17]. EWEs have many important applications ranging from nano-powder synthesis [18,19], inertial confinement fusion through the use of Z-pinches [20,21], rock fracturing [22,23], hypersonic (~3 km/s) jet formation via wire arrays explosions [24–26] and intense point-like sub-nanosecond soft X-ray sources [27,28].

Much of the EWE research has been performed in either vacuum or gaseous environments, where plasma formation along the wire surface and its rapid expansion divert part of the discharge current and limit energy density deposition [29]. Underwater electrical wire explosions (UEWEs) overcome these limitations due to the high breakdown voltage of water (>200 kV/cm), which suppresses the shunting plasma [30], while its low compressibility reduces the expansion velocity (from ~10^6 cm/s to ~10^5 cm/s), enabling

greater energy density deposition into the wire [31]. In recent years, additional exploding conductor geometries have been used to study the mentioned topics, namely exploding metallic foils [32–34] and liners [35], to avoid issues related to the skin effect [33] and instabilities [34,36].

Due to the extreme conditions realized in these explosions (temperatures of several eV, pressures in the range 10^8–10^9 Pa) [3], one of the most notable applications of UEWEs is to verify existing conductivity models [37–39] and equations of state (EOSs) [40,41]. Knowing EOSs is essential for MHD simulations, which use Maxwell's and hydrodynamic equations, circuit equations, conductivity models such as the BKL and QLMD models, and SESAME EOS tables [42–44]. In previous studies of these models using UEWEs [45–50], it was shown that the rate of energy deposition can affect the validity of these EOS and conductivity models, particularly at the sub-microsecond (μs) and nanosecond (ns) energy deposition timescales.

Over the years, many of the parameters affecting the explosion process of wires have been explored. These include the length and cross-section of the wire [51–53], the energy stored in the pulse generator [54], and the type of discharge (underdamped or critically damped) [55]. During our earlier research, most experiments were performed using copper and aluminum wires due to their accessibility and abundant EOS and conductivity data [56–58]. Other metals were later sorted into three groups based on similar current waveforms and thermodynamic properties [51,59–61]. A more detailed review can be found in Ref. [62]. Large surveys of material explosions across different energy deposition timescales in UEWE are challenging due to the need for accurate specific action integral values, which were determined for wire explosions in air and in certain range of current densities [63,64].

In our recent studies on sub-μs underwater explosions of single wires of twelve materials [62], we combined current–voltage diagnostics, laser shadowgraphy of shocks, and one-dimensional hydrodynamic (1DHD) modeling to quantify the deposited energy density, deposition rate, and specific action integral values. It was found that the deposited energy density exceeded the solid–liquid threshold for all materials, yet remained below the level for complete liquid–vapor transition, only surpassing the atomization energy at peak power. The generated plasma was weakly ionized and highly resistive, and materials could be divided into three groups based on the post-peak resistance trend (decrease, plateau, or increase). The maximum observed temperature did not exceed ~6000 K due to the "water bath" effect [65] and the measured strong shock velocities correlated with the simulated wire expansion.

Following this recent research, the present study examines similar materials (Al, Ti, Fe, Ni, Cu, Zn, Mo, Ag, Sn, Ta, Pt, and Au) using a custom-built generator with a μs-scale current rise time (capacitance 10 μF and 3.5 kJ stored energy). The parameters required for a critically damped explosion of wires are determined and compared to the values predicted by the specific current action integral used in electrical explosions studies. Based on current and voltage waveforms, the time-dependent resistance and energy deposition were determined for different materials. This was compared with the onset of weak and strong shock waves, resolved with laser shadowgraphs, to determine the relationship between the phase transition and the observed shocks. The measured velocity of shock waves and wire channel expansion are compared to 1DHD simulations, coupled with SESAME EOS database for most materials.

The remainder of this manuscript is organized as follows. Section 2 describes the experimental setup and the diagnostic methods used in this research. Section 3 summarizes and discusses the experimental and simulation results in Section 3.1, and in

Section 3.2, these are compared with results presented in Ref. [62]. Finally, Section 4 presents the conclusions.

2. Experimental Setup and Diagnostic Methods

Experiments were conducted using a custom-built µs-timescale high-voltage (HV) pulse generator, with 10 µF capacitance. When charged to 27 kV (~3.5 kJ stored energy), the generator delivers ~250 kA to a short-circuit load having an inductance of 15 nH, at a rise time of ~1.1 µs. Current (I) and voltage (V) waveforms were measured using a custom-built, calibrated, self-integrated Rogowski coil (measurement error of ±5%) and a Tektronix P6015A HV divider (measurement error of ±3%, Tektronix, Inc., Beaverton, OR, USA), respectively. The resistive voltage V_r over the load was calculated by subtracting the inductive voltage of the load $V_r = V - L\,dI/dt$. In the latter, L is the inductance of the exploding wire or array, the value of which is estimated with an uncertainty of ≤10%. The contribution of $I\,dL/dt$ in the expression for V_r, is assumed to be negligible due to the logarithmic dependence of L on the expanding radius of the wire. The inductances of the wire or wire array loads were measured during the generator's short-circuit tests with non-exploding wires or wire arrays, when the voltage divider waveform corresponds to $L\,dI/dt$. The difference between the inductance of a single wire and that of a wire array is estimated to be ~10 nH. Indeed, the estimate of $I\,dL/dt$ considering a wire expansion of ~10^3 m/s for ~0.5 µs and with a 100 kA current results in <1 kV, which does not exceed a few percent of the resistive voltage.

The optical setup was similar to that described in Ref. [62] and is presented in Figure 1. Fine metal wires of various materials were stretched between high-voltage (HV) and grounded electrodes, which were fixed to each other using plastic pillars. This design was placed inside a chamber filled with deionized water. One of the two 20 mm thick polymethyl methacrylate (PMMA) windows mounted in the chamber walls allows a continuous-wave (CW) single-mode laser (≤2.5 W, λ = 532 nm) to enter the chamber. The laser beam first passes through a beam expander consisting of two lenses and illuminates the exploding wire. The transmitted light exits through the opposite PMMA window and is collected by an additional lens onto the input slit (10 µm width) of an Optronis Optoscope SC-10 streak camera (Optronis GmbH, Kehl, Germany). Shadow-backlit images are recorded with a CCD size of 1392 × 1080 pixels, corresponding to a total time and spatial scales of either 1.97 µs × 3.8 mm or 4.91 µs × 3.8 mm. The shadow imaging of shock waves was used to determine the onset of the shock wave and its velocity. This method relies on the inclination of the backlighting laser beam on the sharp density gradient at the front of the shock wave. The shock velocities at their onset were obtained from known horizontal (time axis) and vertical (x-axis) scales of the streak shadowgraphy images at $v = dx/dt$. The uncertainty in determining the shock velocity was estimated at ± 50 m/s due to the temporal (±3.6 ns) and spatial (±3.6 µm) resolutions of the streak images and smearing of the shock front. The timing between the HV pulse generator operation, the streak camera and a Tektronix TDS640A oscilloscope (500 MHz, 2 GSa/s, Tektronix, Inc., Beaverton, OR, USA) was obtained using a Stanford DG645 digital delay generator (Stanford Research Systems, Sunnyvale, CA, USA). Additionally, to synchronize the streak images and waveforms of the current and voltage, a Thorlabs NPL52B pulsed laser (532 nm, 10 ns pulse duration, Thorlabs, Inc., Newton, NJ, USA) was used. The laser was triggered by the DG645 generator with a known time delay relative to the HV pulse generator. This laser beam, delivered via an optical fiber, served as a marker in the streak images.

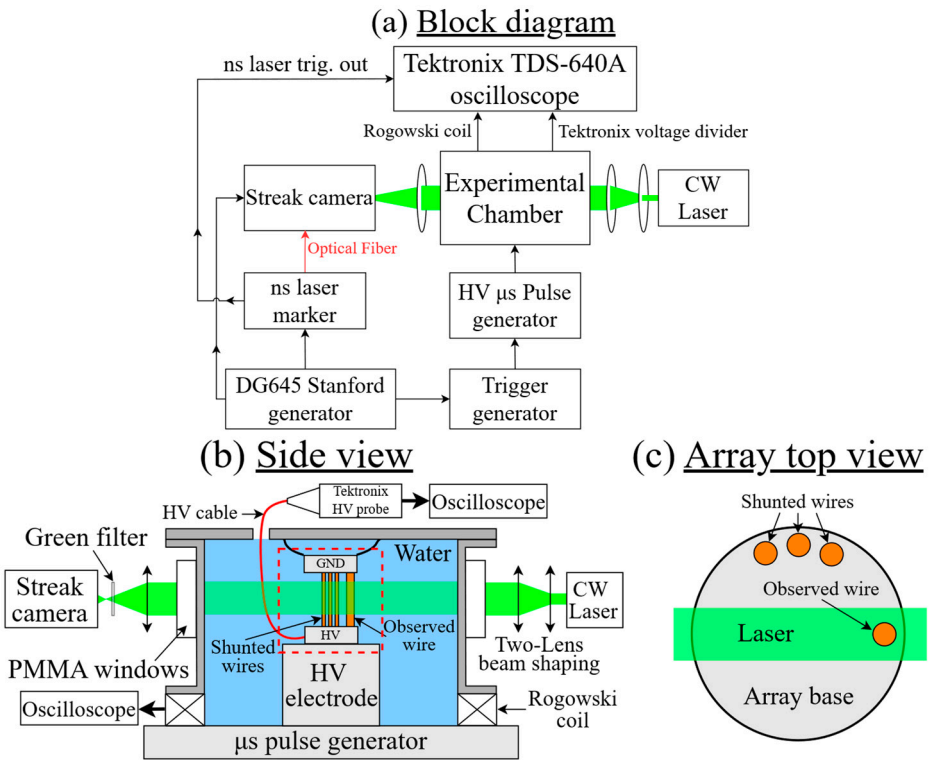

Figure 1. (**a**) Block diagram of the experimental setup. (**b**) Optical setup and experimental chamber. (**c**) Top view of the array with observed and shunted wires, highlighted by a dashed box in (**b**).

Table 1 summarizes the main parameters of the wires used in the present experiments. The dimensions and number of wires for each material were chosen to achieve critically damped explosions, determined by the specific action integral values for each material in vacuum [7]. For every wire material, 2–3 explosions were carried out, showing excellent reproducibility in the results, i.e., identical waveforms of the current, voltage, and shadow images. The skin depth, $\delta(T)$, is evaluated at room and melting temperatures based on the temperature-dependent resistivity [66] $\rho_{res}(T) = \rho_0(1+\alpha T)$ and the generator discharge current pulse rise time $\tau_{rise} \approx 1.1$ µs as $\delta(T) \approx \sqrt{4\pi\rho_{res}(T)\tau_{rise}/\mu_0}$, where μ_0 is the vacuum permeability [62]. This depth becomes comparable to or exceeds the wire radius at the melting temperature owing to the temperature-dependent increase in resistivity. Therefore, the skin effect, which causes uneven current density across the cross-section and, consequently, uneven energy density deposition, is not significant. These findings are supported by our previous research, where microsecond-scale underwater electrical explosions of wires were analyzed using one-dimensional magnetohydrodynamic simulations [52]. The remaining thermophysical properties are provided in our previous publication [62] and are referred to in the text as the tabulated data.

Table 1. Wire samples properties.

Material/Number of Wires	Diameter/Length [mm]	Density [67] [g/cm^3]	Resistivity at Normal Conditions [67] [$\times 10^{-8}$ Ω·m]	Specific Action Integral [7] [$\times 10^9$ A^2·s/cm^4]	Skin Layer at 300 K/at Melting Temperature [66,67] [mm]
Al/1	0.80/40	2.7	2.71	1.8	0.17/0.34
Ti/6	0.20/30	4.51	39.0	0.8	0.66/2.08
Fe/6	0.25/40	7.87	9.87	1.4	0.33/1.09
Ni/5	0.25/40	8.9	7.12	1.9	0.28/0.93
Cu/1	0.60/40	8.96	1.71	4.1	0.14/0.33

Table 1. *Cont.*

Material/Number of Wires	Diameter/Length [mm]	Density [67] [g/cm^3]	Resistivity at Normal Conditions [67] [$\times 10^{-8}$ Ω·m]	Specific Action Integral [7] [$\times 10^9$ A^2·s/cm^4]	Skin Layer at 300 K/at Melting Temperature [66,67] [mm]
Zn/14	0.20/40	7.13	6.01	[1]	0.26/0.42
Mo/2	0.50/30	10.2	5.47	[1]	0.25/0.90
Ag/3	0.38/40	10.5	1.62	2.8	0.13/0.30
Sn/4	0.50/40	7.29	11.5	[1]	0.36/0.50
Ta/4	0.25/40	16.4	13.4	[1]	0.39/1.36
Pt/8	0.30/40	21.5	10.7	[1]	0.35/0.97
Au/5	0.35/40	19.3	2.26	1.8	0.16/0.36

[1] These materials lack specific action integral data in the literature, and therefore, the diameter and number of wires were varied until a nearly critically damped explosion was achieved.

Supplementary one-dimensional hydrodynamical simulations of Euler's equations in a Lagrangian form were carried out for materials with available EOS data [68–70]. For both the wire and water cells, the simulation solves the equations of mass, momentum and energy conservation

$$\frac{\partial \rho}{\partial t} + \vec{\nabla} \cdot \left(\rho \vec{v}\right) = 0, \tag{1}$$

$$\frac{\partial \left(\rho \vec{v}\right)}{\partial t} + \vec{\nabla}\left(\rho \vec{v} \cdot \vec{v}\right) + \vec{\nabla} p = 0, \tag{2}$$

$$\frac{\partial (\rho \epsilon)}{\partial t} + \vec{\nabla} \cdot \left[(\rho \epsilon + p)\vec{v}\right] = 0, \tag{3}$$

where $\rho, \epsilon, \vec{v}, p$ are the density, internal energy, velocity and pressure, respectively. At each time step Δt, Equations (1)–(3) calculate the relations between the density ρ, temperature T, pressure p and internal energy ϵ for each medium from the SESAME EOS [44] tables as $p = p(\rho, T), \epsilon = \epsilon(\rho, T)$. The experimental power $P(t) = I(t)V_r(t)$ is related to the simulation through the internal energy as $\epsilon = P(t)\Delta t$ using Equation (3). At each time step of the simulation, a new value of energy density is deposited into each wire element cell, calculated using experimental data as $dW(t)/dm = (I(t)Vr(t)dt)/m_W$, where m_W is the mass of the wire. This assumes that 100% of the deposited energy transforms into internal energy, neglecting small losses from radiation and thermal conductivity.

From the simulations, the velocities of weak shocks, strong shocks, and wire channel expansion (wire radius) can be compared with the measured shock velocities estimated from streak image data. The validity of this model was supported in earlier publications [69,70], where the experimentally obtained shock wave trajectory was compared with the model's results. Additionally, earlier research [71] showed that, by experimental and 1-D magnetohydrodynamic simulation results, the onset of solid–liquid-vapor phase transitions is accompanied by the generation of weak shock waves. The wire temperature, normally unmeasurable in UEWE due to the bath effect [65], is used to calculate the plasma parameters and the coupling coefficients. Additional information regarding the 1DHD model can be found in Section S1 in the Supplementary Materials.

3. Experimental Results

3.1. UEWE Results Obtained in Experiments Using the μs Timescale Generator

In Figures 2–4, we present shadowgraph streak images of Cu, Ag, and Sn wire explosions, depicting the onset of weak (solid–liquid–vapor) and strong (vapor–plasma) shocks from the initial wire. These are synchronized to waveforms of the measured current,

calculated resistive voltage, effective resistance, power and energy. In most experiments, a critically damped discharge was realized by adjusting the diameter and number of exploding wires, except for Ta and Ti wire explosions. In earlier research [72], it was shown that, for a wire array, the current is evenly distributed among the wires due to positive feedback arising from the increase in resistance during the wire-melting and vaporization phases. Thus, measured quantities are normalized per wire, assuming equal current distribution for each wire. The average rise time of the current across experiments was ~0.92 µs with an average current density of ~0.8 × 10^8 A/cm^2 at maximum current. The wires reach a peak effective resistance of ~0.6 Ω, and the deposited energy density at this time was ~3.4 eV/atom, sufficient for wire vaporization. Results of 1DHD simulations show that at this time, wires expanded by ~40% relative to their original radius, and the temperature reached ~7200 K, comparable with the self-magnetic pressure, indicating the onset of rapid wire expansion. On the other hand, at maximum amplitude of the resistive voltage, the effective resistance reaches extreme values of ~1.4 Ω on average, corresponding to a transition into a resistive weakly ionized plasma. During this moment, the deposited energy density reaches ~9.4 eV/atom and wires expand up to ~170% relative to their original radius. The temperature at this time was ~14,200 K, resulting in thermal pressure (~1.7 GPa) significantly exceeding the pressure of the self-magnetic field (~0.7 GPa).

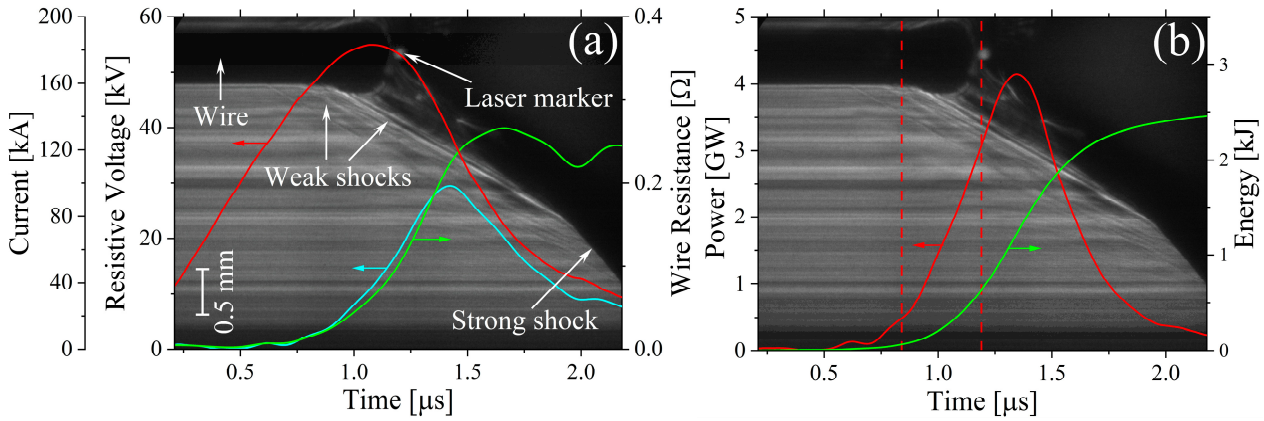

Figure 2. Shadowgraph streak images of a 0.6 mm diameter exploding Cu wire, overlaid with (**a**) waveforms of the current (red), resistive voltage (cyan) effective resistance (green), and (**b**) the power (red) and deposited energy (green). The spatial resolution denoted in (**a**) applies for all images below, and the vertical dashed red lines in (**b**) mark the times for sufficient melting and boiling energy deposition.

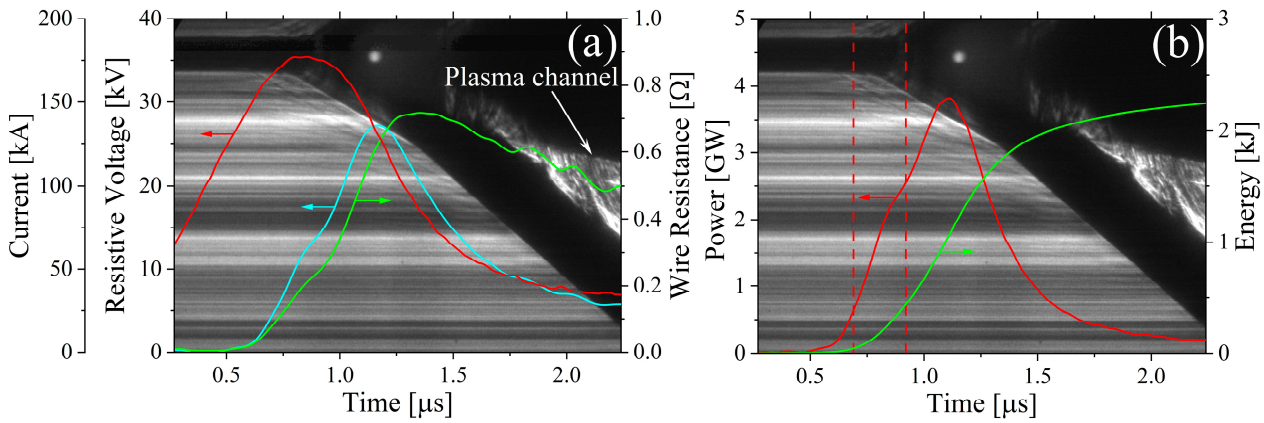

Figure 3. Same as Figure 2 but for an exploding Ag three-wire array, each 0.38 mm in diameter.

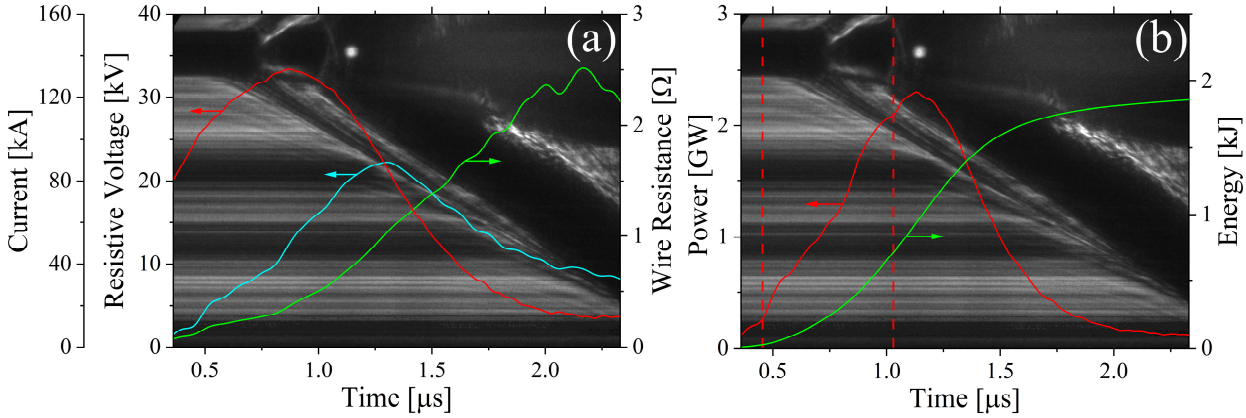

Figure 4. Same as Figure 2 but for an exploding Sn four-wire array, each 0.5 mm in diameter.

In Table 2, we present the calculated energy densities (ϵ_1, ϵ_3) and the tabulated values (ϵ_2, ϵ_4) used for melting and boiling, respectively, together with the enthalpies of melting and vaporization ($\Delta H_f, \Delta H_v$). The values (ϵ_1, ϵ_3) were calculated as $\epsilon_1 = m_W^{-1} \int_0^{t_1} I(\tau) V_r(\tau)\, d\tau$ and $\epsilon_3 = m_W^{-1} \int_{t_1}^{t_2} I(\tau) V_r(\tau)\, d\tau$, where m_W is the mass of the wire, and t_1, t_2 are the onset times of the first (solid–liquid) and second (liquid–vapor) weak shocks. The values (ϵ_1, ϵ_3) were calculated using the specific heat capacity at constant volume C_v and melting and boiling temperatures T_m, T_b of each material using $\epsilon_2 = \int_{T_0}^{T_m} C_v\, dT$ and $\epsilon_4 = \int_{T_m}^{T_b} C_v\, dT$ [62,73–85]. Following the above, in Table 3, we compare the theoretical thermodynamic transition energies to the energies measured in the experiment ϵ_1, ϵ_3 and the skin layer of the material at room temperature and melting. One can see that, for ten out of the twelve tested materials, the experimental melting phase occurs later in time than theoretically predicted by $\left(\epsilon_2 + \Delta H_f\right)/\varepsilon_1$, while for boiling, the tendency is reversed. Notable exceptions are for Ag and Cu, and in some sense for Al wires, which can be explained by the skin effect. The latter leads to the wire experiencing a phase transition before complete melting. These results indicate that magnetic pressure plays a major role in delaying the onset of weak shocks due to melting. A large ratio of energy deposition in the liquid phase $(\epsilon_4 + \Delta H_v)/\varepsilon_3 > 1$ strongly suggests that the onset of the weak shock wave, which relates to the liquid–vapor phase transition, does not occur when the entire wire transforms into vapor, i.e., the coexistence of both phases. The latter is linked to uneven heating of the conductor, which can also be associated with a skin effect. The combined results during the melting and boiling phases confirm the hypothesis of melting retardation by magnetic pressure, leading to two-phase coexistence.

Table 2. Tabulated energy densities ϵ_2, ϵ_4, and enthalpies of melting ΔH_f and vaporization ΔH_v compared to the experimental energy densities ϵ_1 and ϵ_3, calculated from measured waveforms of current and resistive voltage at the observed weak shock onset. Due to measurement errors of the current and voltage waveforms, the uncertainty in the calculated energy density deposition was ±7%. $\epsilon_2, \epsilon_4, \Delta H_f, \Delta H_v$ were calculated based on tabulated data in [62,73–85].

Material	ϵ_1 [J/g]	ϵ_2 [J/g]	ΔH_f [J/g]	ϵ_3 [J/g]	ϵ_4 [J/g]	ΔH_v [J/g]
Ag	130 ± 9	236 ± 1	104 ± 1	1090 ± 80	349 ± 1	2641 ± 8
Cu	370 ± 30	485 ± 1	204 ± 2	1470 ± 100	732 ± 1	5310 ± 27
Au	230 ± 20	142 ± 1	64.6 ± 0.7	150 ± 10	278 ± 1	1870 ± 6
Al	1090 ± 80	644 ± 1	392 ± 5	5000 ± 400	2000 ± 4	12,220 ± 78
Zn	1530 ± 100	899 ± 2	99 ± 2	5700 ± 400	797 ± 2	1995 ± 3
Mo	510 ± 40	169 ± 1	407 ± 16	590 ± 40	234 ± 1	6860 ± 20
Ni	1320 ± 100	744 ± 1	297 ± 3	5700 ± 400	1010 ± 2	7290 ± 34
Fe	1360 ± 100	1012 ± 2	247 ± 5	7700 ± 600	1040 ± 2	7440 ± 22
Pt	430 ± 30	265 ± 1	113 ± 5	2400 ± 200	387 ± 1	2900 ± 10

Table 2. *Cont.*

Material	ϵ_1 [J/g]	ϵ_2 [J/g]	ΔH_f [J/g]	ϵ_3 [J/g]	ϵ_4 [J/g]	ΔH_v [J/g]
Sn	260 ± 20	51 ± 1	60.5 ± 0.1	2100 ± 200	570 ± 1	2540 ± 8
Ti	6200 ± 500	1128 ± 2	300 ± 10	10,500 ± 800	1470 ± 3	9870 ± 21

Table 3. The ratio between tabulated energy densities for solid and liquid phases, in order of increasing electrical resistivity.

Material	$(\epsilon_2+\Delta H_f)/\varepsilon_1$	$(\epsilon_4+\Delta H_v)/\varepsilon_3$	$\Delta_{sk}(T_0)/r_0$	$\Delta_{sk}(T_{melt})/r_0$
Ag	2.62	2.73	0.7	1.6
Cu	1.86	4.12	0.5	1.1
Au	0.89	14.21	0.9	2.1
Al	0.95	2.83	0.4	0.9
Zn	0.85	1.35	1.0	3.6
Mo	0.53	3.75	2.6	4.2
Ni	0.79	1.47	2.2	7.4
Fe	0.93	1.10	2.6	8.7
Pt	0.88	1.39	2.3	6.5
Sn	0.43	1.49	1.4	2.0
Ti	0.23	1.09	6.6	20.8

Shock wave data obtained from experimental shadow streak images and simulations is presented in Figure 5. In our experiments, the solid–liquid–vapor transitions of the wire are first-order phase transitions and are accompanied by a sudden, jump-like increase in volume. This rapid expansion generates a weak shock in the surrounding water, where a weak shock is defined by relatively small jumps in pressure and temperature behind the front, $\frac{\Delta P}{P_0} \ll 1$, $\frac{\Delta T}{T_0} \ll 1$, with P_0 and T_0 denoting the pressure and temperature of the unperturbed medium, and with a Mach number close to unity, $M = 1 + \varepsilon$ with $\varepsilon \ll 1$. Unlike a sound wave, a weak shock is characterized by an increase in entropy across its front, making the process irreversible. The agreement between measured and simulated weak shock velocities was quantified by a root-mean-square (RMS) error of 184 m/s, which is comparable to the combined experimental uncertainty (±50 m/s) and the small absolute deviation of the weak shock velocity from the sound speed in water (~1481 m/s). This level of agreement indicates that the simulations capture the weak-shock regime within the experimental resolution. For strong shock waves, the measured velocities show larger material-dependent variations. The average strong shock wave velocity for most metals was ~2280 m/s, with the highest velocities obtained for Al (~3100 m/s) and Cu (~2900 m/s). These large velocities are consistent with the larger wire channel expansions obtained in simulations for Cu and Al. The corresponding RMS error between measured and simulated strong shock velocities is 390 m/s, reflecting the increased sensitivity of the strong shock regime to the details of energy deposition and channel expansion. Using Hugoniot relations for water [86,87], the velocity, pressure, and density behind the strong shock front are estimated as $u_p \approx 750$ m/s, $p \approx 2.3 \times 10^9$ Pa and $\rho \approx 1.34$ g/cm^3. The notable exception in the simulated velocities for Ta can be the result of the underdamped explosion realized in this experiment.

Lastly, an analysis of the plasma parameters, namely the electron density n_e, ionization degree η, simulated temperatures T_{sim}, and plasma ideality Γ_{sim}, estimated using the same workflow as described in Ref. [62], is presented in Table 4. Here, n_e and η were estimated using experimentally measured resistive voltage and electron current velocity. This enables one to estimate the plasma ideality parameter, yielding $\Gamma_{sim} \geq 1$, except for the Al wire explosion, where $\Gamma_{sim} = 0.94$. In Table S1 (see Supplementary Materials), the approximated

temperature T_{Saha}, obtained from the Saha equation with the estimated values of n_e and its corresponding value of Γ_{Saha}, can be seen. It is evident that the values of T_{sim} are larger than T_{Saha}, leading to slightly smaller values of Γ_{sim} compared to Γ_{Saha}. Considering that the Saha equation can only be applied to ideal plasma and is merely a rough approximation under these conditions, these results suggest that, in the case of wire explosion, this approach must be used with great caution.

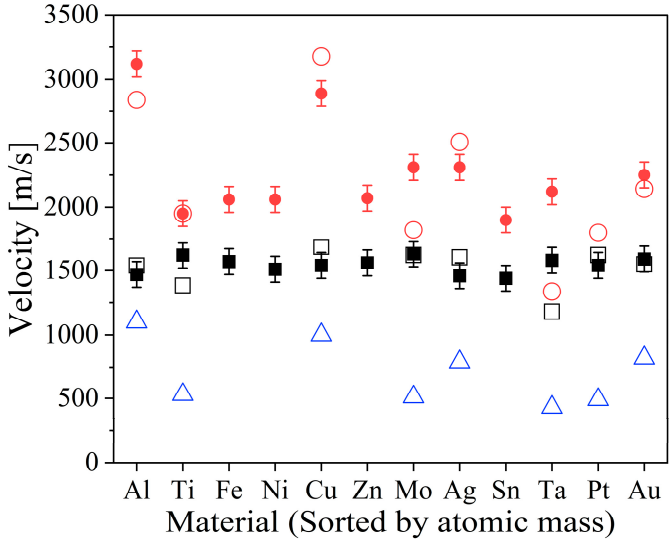

Figure 5. Comparison of weak shock (black filled squares) and strong shock (red filled circles) to simulation results (corresponding hollow shapes) for different materials. The average velocity of the simulated wire channel expansion for each material (blue hollow triangle) is also shown.

Table 4. Calculated and simulated plasma parameters.

Material	n_e [$\times 10^{20}$ cm^{-3}]	η	T_{sim} [eV]	Γ_{sim}
Al	2.4	0.02	1.54	0.94
Ti	3.3	0.02	1.11	1.45
Cu	4.4	0.04	1.71	1.04
Mo	8.0	0.04	1.36	1.59
Ag	2.5	0.04	1.34	1.09
Ta	17.0	0.07	1.12	2.46
Pt	2.0	0.03	0.70	1.94
Au	1.6	0.03	0.91	1.40
Average	5.2	0.036	1.22	1.49

3.2. Comparison with Previous Results Obtained on the Sub-μs Timescale

In Tables 5 and 6, we present a detailed comparison of the results from this study with those from the sub-μs regime [62]. We compare the measured effective resistances, the observed phase transitions and shock waves, the calculated action integral values and the plasma parameters. One can see that the main difference between these experiments is the energy density deposition rate, which is significantly higher for sub-μs timescale explosions. The average deposited energy density was higher for sub-μs explosions. Another substantial difference lies in the specific action integrals at the maximal discharge current, despite similar current densities for both types of explosions. These were calculated as $h = S^{-2}\int_0^{\tau_{max}} I^2(t)dt$, where S is the wire's cross-sectional area, $I(t)$ is the current flowing through the wire, and τ_{max} is the time when the current reaches its maximum amplitude and then begins to decrease. At that moment, the wire undergoes a vapor-to-high-resistance-

plasma phase transition, and the main energy deposition begins, accompanied by rapid radial wire expansion as the magnetic pressure of the discharge current becomes smaller than the internal pressure. It is important to note that the absence of magnetic pressure in 1DHD simulations provides an incomplete view of the explosion process, as this pressure plays a role in confining the wire. Lastly, one can see that skin effects are not pronounced in μs-timescale explosions.

Table 5. Average values obtained on different timescale explosions.

Parameter	Sub-μs Timescale Explosions		μs Timescale Explosions	
	at I_{max}	at φ_{max}	at I_{max}	at φ_{max}
Current density [$\times 10^8$ A/cm^2]	0.6	0.3	0.8	0.2
Average deposited energy density [eV/atom]	5.5	12.6	3.4	9.4
Energy density deposition rate [$\times 10^9$ J/(g·s)]	37.9	67.8	5.64	10.2
Average effective resistance [Ω]	0.7	1.1	0.6	1.4
Specific action integrals [$\times 10^9$ A^2 s/cm^4]	0.8	0.9	4.8	0.5
Average radial expansion velocity of the wire [m/s]	870		710	
Ratio of average skin layer to wire radius	At room temperature: 1.1 At maximum current: 8.6		At room temperature: 2.0 At maximum current: 11.9	

Table 6. Quantitative comparison between the results obtained in sub-μs and μs timescale UEWE.

Parameter	Sub-μs Timescale Explosions	μs Timescale Explosions
Effective Resistance	Materials were classified as having a peak (Al, Ag, Zn, Ni), quasi-plateau (Cu, Fe, Ti, Mo, Ta), or continuously rising (Sn, Pt, Au) resistance, explained by the interplay between electron avalanching, induced voltage and the geometry of the wire and the remaining energy in the pulse generator.	Most materials display a notable resistance peak (Ti, Fe, Ni, Zn, Ag, Sn, Ta, Au) compared to a quasi-plateau (Cu, Mo) or a continuously rising (Al, Pt) resistance. This suggests that plasma forms in a similar manner, yielding nearly identical resistance even under different energy deposition rates.
Energy deposition in the solid phase	The solid–liquid phase transition shock waves are delayed for most materials compared to the deposited energy required for this transition. This was explained by strong magnetic pressure, which prevents expansion of the wire.	As in the sub-μs timescale, the solid–liquid phase transition appears later than predicted by thermodynamic calculations, except for the thicker Cu and Al wires. These exceptions may be linked to the skin effect and indicate solid–liquid phase coexistence in these materials.
Energy deposition in the liquid phase	When liquid–vapor weak shocks are observed, only a small fraction of the energy required for this transition is deposited in the wires, suggesting that phase coexistence occurs. The average ratio between deposited and required energy for this transition is for all studied wire explosions $\langle(\epsilon_4 + \Delta H_v)/\varepsilon_3\rangle \approx 7.1$.	Similar behavior is observed, with an average energy deposition ratio of $\langle(\epsilon_4 + \Delta H_v)/\varepsilon_3\rangle \approx 3.2$. This indicates that a larger fraction of the wire exists as vapor in this regime, which may arise from a less pronounced skin effect.

Table 6. *Cont.*

Parameter	Sub-μs Timescale Explosions	μs Timescale Explosions
Specific action integral values	Values of the specific action integrals are lower than those reported for wire explosions in vacuum and air, due to the absence of surface breakdown around the wire and the slow expanding radius caused by underwater experiments. The average ratios between reported and measured values are $\langle h/h_{I_{max}} \rangle \approx 2.8$ at peak current and $\langle h/h_{\varphi_{max}} \rangle \approx 2.6$ at peak resistive voltage.	Here an even larger discrepancy exists between the values of the specific action integrals compared to those obtained in vacuum and air. The average ratio between reported and measured values are $\langle h/h_{I_{max}} \rangle \approx 3.5$ at peak current and $\langle h/h_{\varphi_{max}} \rangle \approx 31$ at peak resistive voltage. The latter, obtained for Al and Cu wire explosions, could be associated with the significantly larger expansion in vacuum, which results in a larger value of $h \propto r^{-4}$.
Shock wave velocities	Weak shock velocities are found to be similar and follow the water sound velocity, while the average SSW velocity is ~2600 m/s. The fastest velocities were measured for Cu, Al, Pt, Ag, and Zn, corresponding to a higher radial wire expansion velocity (>1000 m/s) and possible partial combustion of Al wires.	A comparable result was obtained for weak shocks, while the average SSW velocity is lower and does not exceed ~2300 m/s. The latter may stem from the overall smaller energy density deposition rate, which results in a smaller velocity of the wire radial expansion. Cu, Al, Ag, Au and Mo created the fastest SSW comparable with those obtained in sub-μs explosions, potentially due to their higher vapor content during the onset of the SSW (i.e., higher $(\epsilon_4 + \Delta H_v)/\varepsilon_3$; see Table 3) and the highest radial expansion (~1000 m/s, compared to other materials with <800 m/s).
Plasma parameters	The plasma formed at maximum resistive voltage, i.e., transition to low-ionized plasma, has an average electron density $\langle n_e \rangle \approx 1.3 \times 10^{20}$ cm^{-3} ionization rate of ~9% and temperatures reaching ~2.1 eV. Hence, plasma formed in these explosions is weakly ionized and non-ideal $\langle \Gamma \rangle \approx 1$).	The plasma created during peak resistive voltage is non-ideal; however, with overall lower electron density $\langle n_e \rangle \approx 5.2 \times 10^{20}$ cm^{-3}, a smaller ionization degree of ~4% and a temperature that does not exceed ~1.2 eV. This can be explained by the smaller energy density deposited into the wires.

4. Conclusions

UEWE experiments carried out on the μs timescale showed many similarities with sub-μs timescale results reported in Ref. [62], despite the significantly smaller energy deposition rate. On the sub-μs timescale, the solid–liquid phase transition occurs later than predicted by thermodynamic calculations due to self-magnetic-field pressure, which delays it. Contrarily, the liquid–vapor transition occurs when only a small fraction of the energy required for this transition is deposited into the wires, indicating the co-existence of the two phases. Similarly to the sub-μs timescale, all studied materials can be divided into three groups, having (a) a resistance peak (Ti, Fe, Ni, Zn, Ag, Sn, Ta, Au); (b) a resistance quasi-plateau (Cu, Mo), or (c) a continuous rise in resistance (Al, Pt). Additionally, the plasma created at peak resistive voltage was found to be non-ideal, but with a lower electron density, smaller ionization degree, and colder temperature. Finally, a larger discrepancy was found again between the specific action integral measured in this study and the values reported for wire explosions in vacuum.

Supplementary Materials: The following supporting information can be downloaded at https://www.mdpi.com/article/10.3390/plasma9010007/s1. Table S1: Calculated plasma parameters

using the Saha equation for the experimental electron density n_e. Section S1: Boundary and Initial conditions of the 1DHD model.

Author Contributions: Conceptualization, R.G. and Y.E.K.; methodology, R.G. and Y.E.K.; software, R.G. and N.A.; validation, R.G. and Y.E.K.; formal analysis, R.G. and Y.E.K.; investigation, R.G. and S.E.; resources, Y.E.K.; data curation, R.G. and S.E.; writing—original draft preparation, R.G. and Y.E.K.; writing—review and editing, R.G. and Y.E.K.; visualization, R.G.; supervision, Y.E.K.; project administration, R.G. and Y.E.K.; funding acquisition, Y.E.K. All authors have read and agreed to the published version of the manuscript.

Funding: This research was funded by the Israel Science Foundation, grant number 418/22.

Institutional Review Board Statement: Not applicable.

Informed Consent Statement: Not applicable.

Data Availability Statement: Data from this experiment (raw shadowgraphy images, waveforms, simulation results, and tables) can be obtained from the corresponding author.

Acknowledgments: We are grateful to J. Leopold for fruitful discussions.

Conflicts of Interest: The authors declare no conflicts of interest.

References

1. Committee on High Energy Density Plasma Physics. *Frontiers in High Energy Density Physics*; National Academies Press: Washington, DC, USA, 2003.
2. Fortov, V.E.; Iakubov, I.T. *The Physics of Non-Ideal Plasma*; World Scientific: Singapore, 2000.
3. Drake, R.P. *High-Energy-Density Physics: Fundamentals, Inertial Fusion, and Experimental Astrophysics*; Shock Wave and High Pressure Phenomena; Springer: Berlin/Heidelberg, Germany; New York, NY, USA, 2006.
4. Chace, W.G.; Moore, H.K. (Eds.) *Exploding Wires: Volumes 1–4*; Plenum Press: New York, NY, USA, 1959.
5. Luchinskii, A.V. *Electrical Explosions of Conductors*; Nauka: Moscow, Russia, 1989.
6. Chace, W.G. Exploding Wires. *Phys. Today* **1964**, *17*, 19–24. [CrossRef]
7. Oreshkin, V.I.; Baksht, R.B. Wire Explosion in Vacuum. *IEEE Trans. Plasma Sci.* **2020**, *48*, 1214–1248. [CrossRef]
8. Abramova, K.B.; Zlatin, N.A.; Peregud, B.P. Magnetohydrodynamic Instability of Liquid and Solid Conductors—Destruction of Conductors by an Electric Current. *J. Exp. Theor. Phys.* **1975**, *69*, 2007–2022.
9. Oreshkin, V.I.; Baksht, R.B.; Ratakhin, N.A.; Shishlov, A.V.; Khishchenko, K.V.; Levashov, P.R.; Beilis, I.I. Wire Explosion in Vacuum: Simulation of a Striation Appearance. *Phys. Plasmas* **2004**, *11*, 4771–4776. [CrossRef]
10. Peterson, K.J.; Sinars, D.B.; Yu, E.P.; Herrmann, M.C.; Cuneo, M.E.; Slutz, S.A.; Smith, I.C.; Atherton, B.W.; Knudson, M.D.; Nakhleh, C. Electrothermal Instability Growth in Magnetically Driven Pulsed Power Liners. *Phys. Plasmas* **2012**, *19*, 092701. [CrossRef]
11. Yu, E.P.; Awe, T.J.; Cochrane, K.R.; Peterson, K.J.; Yates, K.C.; Hutchinson, T.M.; Hatch, M.W.; Bauer, B.S.; Tomlinson, K.; Sinars, D.B. Seeding the Electrothermal Instability through a Three-Dimensional, Nonlinear Perturbation. *Phys. Rev. Lett.* **2023**, *130*, 255101. [CrossRef]
12. Oreshkin, V.I. The Development of Overheat Instabilities in a Metastable Metal. *Tech. Phys. Lett.* **2018**, *44*, 930–933. [CrossRef]
13. Bennett, F.D. Cylindrical Shock Waves from Exploding Wires. *Phys. Fluids* **1958**, *1*, 347–352. [CrossRef]
14. Fedotov-Gefen, A.; Efimov, S.; Gilburd, L.; Bazalitski, G.; Gurovich, V.T.; Krasik, Y.E. Generation of a 400 GPa Pressure in Water Using Converging Strong Shock Waves. *Phys. Plasmas* **2011**, *18*, 062701. [CrossRef]
15. Lisitsyn, I.V.; Muraki, T.; Akiyama, H. Mechanism of Shock Waves Generation and Material Destruction in a Wire Induced Surface Flashover. *Phys. B Condens. Matter* **1997**, *239*, 6–8. [CrossRef]
16. Li, L.; Qian, D.; Zou, X.; Wang, X. Underwater Electrical Wire Explosion: Shock Wave from Melting Being Overtaken by Shock Wave from Vaporization. *Phys. Plasmas* **2018**, *25*, 53502. [CrossRef]
17. Shi, H.; Yin, G.; Fan, Y.; Wu, J.; Li, X.; Murphy, A.B. Multilayer Weak Shocks Generated by Restrike during Underwater Electrical Explosion of Cu Wires. *Appl. Phys. Lett.* **2019**, *115*, 84101. [CrossRef]
18. Kotov, Y.A. Electric Explosion of Wires as a Method for Preparation of Nanopowders. *J. Nanopart. Res.* **2003**, *5*, 539–550. [CrossRef]
19. Égerházi, L.; Szörényi, T. The Potential of Wire Explosion in Nanoparticle Production in Terms of Reproducibility. *Materials* **2024**, *17*, 3450. [CrossRef]

20. Burdiak, G.C.; Lebedev, S.V.; Suzuki-Vidal, F.; Swadling, G.F.; Bland, S.N.; Niasse, N.; Suttle, L.; Bennet, M.; Hare, J.; Weinwurm, M.; et al. Cylindrical Liner Z-Pinch Experiments for Fusion Research and High-Energy-Density Physics. *J. Plasma Phys.* **2015**, *81*, 365810301. [CrossRef]
21. Qi, J.M.; Wang, Z.; Chu, Y.Y.; Li, Z.H. Simulations of Fusion Chamber Dynamics and First Wall Response in a Z-Pinch Driven Fusion–Fission Hybrid Power Reactor (Z-FFR). *Fusion Eng. Des.* **2016**, *104*, 61–70. [CrossRef]
22. Meng, Y.; Jin, W.; Zhang, K.; Ding, W.; Zhang, Y. Shock Wave Generated by Composite Energetic Material Driven by Electrical Non-Penetrating Wire Explosion Plasma. *Rev. Sci. Instrum.* **2024**, *95*, 093504. [CrossRef] [PubMed]
23. Meng, B.; Cao, Y.; Zhang, X.; Chang, L.; Zhang, J.; Shi, B.; Guo, S.; Ma, Z. Pulse Wave and Rock Fracturing Characteristics of Composite Energetic Materials Ignited by Underwater Wire Electrical Explosion. *ACS Omega* **2025**, *10*, 19350–19360. [CrossRef] [PubMed]
24. Maler, D.; Kozlov, M.; Efimov, S.; Krasik, Y.E. Supersonic Jet Generation by Underwater Sub-Microsecond Electrical Explosions of Wire Arrays. *Phys. Plasmas* **2022**, *29*, 032705. [CrossRef]
25. Strucka, J.; Lukic, B.; Koerner, M.; Halliday, J.W.D.; Yao, Y.; Mughal, K.; Maler, D.; Efimov, S.; Skidmore, J.; Rack, A.; et al. Synchrotron Radiography of Richtmyer–Meshkov Instability Driven by Exploding Wire Arrays. *Phys. Fluids* **2023**, *35*, 044108. [CrossRef]
26. Liu, Z.; Shi, H.; Qian, D.; Li, L.; Wang, X.; Zou, X. Underwater Electrical Wire Array Explosion: Fundamentals, Design, and Applications. *J. Phys. D Appl. Phys.* **2026**, *59*, 023004. [CrossRef]
27. Shelkovenko, T.A.; Sinars, D.B.; Pikuz, S.A.; Chandler, K.M.; Hammer, D.A. Point-Projection x-Ray Radiography Using an X Pinch as the Radiation Source. *Rev. Sci. Instrum.* **2001**, *72*, 667–670. [CrossRef]
28. Strucka, J.; Halliday, J.W.D.; Gheorghiu, T.; Horton, H.; Krawczyk, B.; Moloney, P.; Parker, S.; Rowland, G.; Schwartz, N.; Stanislaus, S.; et al. A Portable X-Pinch Design for x-Ray Diagnostics of Warm Dense Matter. *Matter Radiat. Extrem.* **2022**, *7*, 016901. [CrossRef]
29. Oreshkin, V.I.; Khishchenko, K.V.; Levashov, P.R.; Rousskikh, A.G.; Chaikovskii, S.A. Strata Formation at Fast Electrical Explosion of Cylindrical Conductors. *High Temp.* **2012**, *50*, 584–595. [CrossRef]
30. Ivanenkov, G.V.; Gus'kov, S.Y.; Barishpol'tsev, D.V. Current Shunting and Formation of Stationary Shock Waves during Electric Explosions of Metal Wires in Air. *Plasma Phys. Rep.* **2010**, *36*, 67–76. [CrossRef]
31. Edelson, H.D.; Korneff, T. A Comparative Study of Exploding Wires in Air and Water. *J. Appl. Phys.* **1966**, *37*, 2166–2168. [CrossRef]
32. Maisonnier, C.; Linhart, J.G.; Gourlan, C. Rapid Transfer of Magnetic Energy by Means of Exploding Foils. *Rev. Sci. Instrum.* **1966**, *37*, 1380–1384. [CrossRef]
33. Sarkisov, G.S.; Rosenthal, S.E.; Struve, K.W. Thermodynamical Calculation of Metal Heating in Nanosecond Exploding Wire and Foil Experiments. *Rev. Sci. Instrum.* **2007**, *78*, 43505. [CrossRef]
34. Steiner, A.M.; Campbell, P.C.; Yager-Elorriaga, D.A.; Jordan, N.M.; Mcbride, R.D.; Lau, Y.Y.; Gilgenbach, R.M. The Electrothermal Instability on Pulsed Power Ablations of Thin Foils. *IEEE Trans. Plasma Sci.* **2018**, *46*, 3753–3765. [CrossRef]
35. Awe, T.J.; Peterson, K.J.; Yu, E.P.; McBride, R.D.; Sinars, D.B.; Gomez, M.R.; Jennings, C.A.; Martin, M.R.; Rosenthal, S.E.; Schroen, D.G.; et al. Experimental Demonstration of the Stabilizing Effect of Dielectric Coatings on Magnetically Accelerated Imploding Metallic Liners. *Phys. Rev. Lett.* **2016**, *116*, 065001. [CrossRef]
36. Steiner, A.M.; Campbell, P.C.; Yager-Elorriaga, D.A.; Cochrane, K.R.; Mattsson, T.R.; Jordan, N.M.; McBride, R.D.; Lau, Y.Y.; Gilgenbach, R.M. The Electro-Thermal Stability of Tantalum Relative to Aluminum and Titanium in Cylindrical Liner Ablation Experiments at 550 kA. *Phys. Plasmas* **2018**, *25*, 032701. [CrossRef]
37. DeSilva, A.W.; Katsouros, J.D. Measurement of the Electrical Conductivity of Metals in the Vicinity of the Critical Point. *Int. J. Thermophys.* **1999**, *20*, 1267–1277. [CrossRef]
38. DeSilva, A.W.; Vunni, G.B. Electrical Conductivity of Dense Al, Ti, Fe, Ni, Cu, Mo, Ta, and W Plasmas. *Phys. Rev. E* **2011**, *83*, 037402. [CrossRef]
39. Apfelbaum, E.M. The Pressure, Internal Energy, and Conductivity of Tantalum Plasma. *Contrib. Plasma Phys.* **2017**, *57*, 479–485. [CrossRef]
40. Fortov, V.E.; Khishchenko, K.V.; Levashov, P.R.; Lomonosov, I.V. Wide-Range Multi-Phase Equations of State for Metals. *Nucl. Instrum. Methods Phys. Res. Sect. A Accel. Spectrometers Detect. Assoc. Equip.* **1998**, *415*, 604–608. [CrossRef]
41. Barysevich, A.E.; Cherkas, S.L. Testing the Equation of State and Electrical Conductivity of Copper by the Electrical Wire Explosion in Air: Experiment and Magnetohydrodynamic Simulation. *Phys. Plasmas* **2011**, *18*, 052703. [CrossRef]
42. Bakulin, Y.D.; Kuropatenko, V.F.; Luchinskii, A.V. MHD (Magnetohydrodynamical) Calculation for Exploding Wires. *J. Tech. Phys.* **1976**, *21*, 1144–1147.
43. Desjarlais, M.P. Practical Improvements to the Lee-More Conductiv-Ity Near the Metal-Insulator Transition. *Contrib. Plasma Phys.* **2001**, *41*, 270. [CrossRef]

44. Lyon, S.P.; Johnson, J. *SESAME: The Los Alamos National Laboratory Equation of State Database*; Report no. LA-UR-92-3407; Los Alamos National Laboratory: Los Alamos, NM, USA, 1992.
45. Lee, Y.T.; More, R.M. An Electron Conductivity Model for Dense Plasmas. *Phys. Fluids* **1984**, *27*, 1273–1286. [CrossRef]
46. DeSilva, A.W.; Kunze, H.J. Experimental Study of the Electrical Conductivity of Strongly Coupled Copper Plasmas. *Phys. Rev. E* **1994**, *49*, 4448. [CrossRef]
47. Redmer, R. Electrical Conductivity of Dense Metal Plasmas. *Phys. Rev. E* **1999**, *59*, 1073. [CrossRef]
48. Desjarlais, M.P.; Kress, J.D.; Collins, L.A. Electrical Conductivity for Warm, Dense Aluminum Plasmas and Liquids. *Phys. Rev. E* **2002**, *66*, 025401. [CrossRef]
49. Oreshkin, V.I.; Baksht, R.B.; Labetsky, A.Y.; Rousskikh, A.G.; Shishlov, A.V.; Levashov, P.R.; Khishchenko, K.V.; Glazyrin, I.V. Study of Metal Conductivity near the Critical Point Using a Microwire Electrical Explosion in Water. *Tech. Phys.* **2004**, *49*, 843–848. [CrossRef]
50. Sheftman, D.; Shafer, D.; Efimov, S.; Krasik, Y.E. Evaluation of Electrical Conductivity of Cu and Al through Sub Microsecond Underwater Electrical Wire Explosion. *Phys. Plasmas* **2012**, *19*, 034501. [CrossRef]
51. Romanova, V.M.; Pikuz, S.A.; Ter-Oganesyan, A.E.; Mingaleev, A.R.; Shelkovenko, T.A.; Tkachenko, S.I. Nanosecond Electrical Explosion of Micron Diameter Wire. *Czechoslov. J. Phys.* **2006**, *56*, B349–B356. [CrossRef]
52. Virozub, A.; Gurovich, V.T.; Yanuka, D.; Antonov, O.; Krasik, Y.E. Addressing Optimal Underwater Electrical Explosion of a Wire. *Phys. Plasmas* **2016**, *23*, 092708. [CrossRef]
53. Maler, D.; Liverts, M.; Efimov, S.; Virozub, A.; Krasik, Y.E. Addressing the Critical Parameters for Overdamped Underwater Electrical Explosion of Wire. *Phys. Plasmas* **2022**, *29*, 102703. [CrossRef]
54. Han, R.; Wu, J.; Zhou, H.; Zhang, Y.; Qiu, A.; Yan, J.; Ding, W.; Li, C.; Zhang, C.; Ouyang, J. Experiments on the Characteristics of Underwater Electrical Wire Explosions for Reservoir Stimulation. *Matter Radiat. Extrem.* **2020**, *5*, 047201. [CrossRef]
55. Han, R.; Wu, J.; Zhou, H.; Ding, W.; Qiu, A.; Clayson, T.; Wang, Y.; Ren, H. Characteristics of Exploding Metal Wires in Water with Three Discharge Types. *J. Appl. Phys.* **2017**, *122*, 33302. [CrossRef]
56. Sasaki, T.; Nakajima, M.; Kawamura, T.; Horioka, K. Electrical Conductivities of Aluminum, Copper, and Tungsten Observed by an Underwater Explosion. *Phys. Plasmas* **2010**, *17*, 084501. [CrossRef]
57. Bennett, F.D. High-Temperature Exploding Wires. In *Progress in High Temperature Physics and Chemistry: Volume 2*; Rouse, C.A., Ed.; Pergamon: London, UK, 1968; pp. 1–63.
58. Peterson, K.J.; Yu, E.P.; Sinars, D.B.; Cuneo, M.E.; Slutz, S.A.; Koning, J.M.; Marinak, M.M.; Nakhleh, C.; Herrmann, M.C. Simulations of Electrothermal Instability Growth in Solid Aluminum Rods. *Phys. Plasmas* **2013**, *20*, 056305. [CrossRef]
59. Romanova, V.M.; Ivanenkov, G.V.; Mingaleev, A.R.; Ter-Oganesyan, A.E.; Shelkovenko, T.A.; Pikuz, S.A. Electric Explosion of Fine Wires: Three Groups of Materials. *Plasma Phys. Rep.* **2015**, *41*, 617–636. [CrossRef]
60. Han, R.; Wu, J.; Qiu, A.; Ding, W.; Zhang, Y. Electrical Explosions of Al, Ti, Fe, Ni, Cu, Nb, Mo, Ag, Ta, W, W-Re, Pt, and Au Wires in Water: A Comparison Study. *J. Appl. Phys.* **2018**, *124*, 043302. [CrossRef]
61. Romanova, V.M.; Tilikin, I.N.; Ter-Oganesyan, A.E.; Rodionov, A.A.; Mingaleev, A.R.; Shelkovenko, T.A.; Pikuz, S.A. Features of the Explosion of Conductors from Various Materials Based on Electrotechnical Measurements. *Plasma Phys. Rep.* **2025**, *51*, 1211–1221. [CrossRef]
62. Grikshtas, R.; Asmedianov, N.; Maler, D.; Efimov, S.; Krasik, Y.E. Electrical Properties of Different Materials Studied by Sub-Microsecond Underwater Electrical Explosions of Single Wires. *Phys. Plasmas* **2024**, *31*, 063502. [CrossRef]
63. Sedoi, V.S. The Current Density and the Specific Energy Input in Fast Electrical Explosion. *IEEE Trans. Plasma Sci.* **1999**, *27*, 845–850. [CrossRef]
64. Oreshkin, V.I.; Barengol'Ts, S.A.; Chaikovsky, S.A. Numerical Calculation of the Current Specific Action Integral at the Electrical Explosion of Wires. *Tech. Phys.* **2007**, *52*, 642–650. [CrossRef]
65. Oreshkin, V.I.; Chaikovsky, S.A.; Ratakhin, N.A.; Grinenko, A.; Krasik, Y.E. "Water Bath" Effect during the Electrical Underwater Wire Explosion. *Phys. Plasmas* **2007**, *14*, 102703. [CrossRef]
66. Grigoriev, I.S.; Melikhov, E.Z. *Physical Values (in Russian)*; Energoatomizdat: Moscow, Russia, 1991.
67. Chemical Rubber Company. *CRC Handbook of Chemistry and Physics: A Ready-Reference Book of Chemical and Physical Data*, 84th ed.; Lide, D.R., Ed.; CRC Press: Boca Raton, FL, USA, 2003.
68. Maler, D.; Grikshtas, R.; Efimov, S.; Merzlikin, L.; Liverts, M.; Kozlov, M.; Krasik, Y.E. Supersonic Water Jets as Point-like Sources of Extremely High Pressure. *Phys. Plasmas* **2023**, *30*, 022710. [CrossRef]
69. Bazalitski, G.; Gurovich, V.T.; Fedotov-Gefen, A.; Efimov, S.; Krasik, Y.E. Simulation of Converging Cylindrical GPa-Range Shock Waves Generated by Wire Array Underwater Electrical Explosions. *Shock Waves* **2011**, *21*, 321–329. [CrossRef]
70. Fedotov-Gefen, A.; Efimov, S.; Gilburd, L.; Gleizer, S.; Bazalitsky, G.; Gurovich, V.T.; Krasik, Y.E. Extreme Water State Produced by Underwater Wire-Array Electrical Explosion. *Appl. Phys. Lett.* **2010**, *96*, 221502. [CrossRef]
71. Rososhek, A.; Efimov, S.; Tewari, S.V.; Yanuka, D.; Krasik, Y.E. Phase Transitions of Copper, Aluminum, and Tungsten Wires during Underwater Electrical Explosions. *Phys. Plasmas* **2018**, *25*, 102709. [CrossRef]

72. Rososhek, A.; Efimov, S.; Virozub, A.; Maler, D.; Krasik, Y.E. Particularities of Shocks Generated by Underwater Electrical Explosions of a Single Wire and Wire Arrays. *Appl. Phys. Lett.* **2019**, *115*, 074101. [CrossRef]
73. Arblaster, J.W. Thermodynamic Properties of Gold. *J. Phase Equilibria Diffus.* **2016**, *37*, 229–245. [CrossRef]
74. Arblaster, J.W. Thermodynamic Properties of Silver. *J. Phase Equilibria Diffus.* **2015**, *36*, 573–591. [CrossRef]
75. Arblaster, J.W. Thermodynamic Properties of Tantalum. *J. Phase Equilibria Diffus.* **2018**, *39*, 255–272. [CrossRef]
76. Arblaster, J.W. Thermodynamic Properties of Copper. *J. Phase Equilibria Diffus.* **2015**, *36*, 422–444. [CrossRef]
77. Arblaster, J.W. Thermodynamic Properties of Tungsten. *J. Phase Equilibria Diffus.* **2018**, *39*, 891–907. [CrossRef]
78. Desai, P.D. Thermodynamic Properties of Titanium. *Int. J. Thermophys.* **1987**, *8*, 781–794. [CrossRef]
79. Desai, P.D. Thermodynamic Properties of Nickel. *Int. J. Thermophys.* **1987**, *8*, 763–780. [CrossRef]
80. Desai, P.D. Thermodynamic Properties of Manganese and Molybdenum. *J. Phys. Chem. Ref. Data* **1987**, *16*, 91–108. [CrossRef]
81. Desai, P.D. Thermodynamic Properties of Iron and Silicon. *J. Phys. Chem. Ref. Data* **1986**, *15*, 967–983. [CrossRef]
82. Desai, P.D. Thermodynamic Properties of Aluminum. *Int. J. Thermophys.* **1987**, *8*, 621–638. [CrossRef]
83. Brewer, L.; Porter, R.F. The Heat of Sublimation of Tin and the Dissociation Energy of SnO. *J. Chem. Phys.* **1953**, *21*, 2012–2013. [CrossRef]
84. Binnewies, M.; Milke, E. *Thermochemical Data of Elements and Compounds: Second, Revised and Extended Edition*; Wiley Blackwell: Hoboken, NJ, USA, 2008.
85. Arblaster, J.W. The Thermodynamic Properties of Platinum: Revised Data for The Liquid State and Vapour Pressure. *Platin. Met. Rev.* **2005**, *49*, 141–149. [CrossRef]
86. Zel'dovich, Y.B.; Raizer, Y.P. *Shock Waves and High-Temperature Hydrodynamic Phenomena*; Academic Press: New York, NY, USA, 1966; Volume 1.
87. Takayama, K.; Igra, O. (Eds.) *Frontiers of Shock Wave Research*; Springer International Publishing: Cham, Switzerland, 2022.

Disclaimer/Publisher's Note: The statements, opinions and data contained in all publications are solely those of the individual author(s) and contributor(s) and not of MDPI and/or the editor(s). MDPI and/or the editor(s) disclaim responsibility for any injury to people or property resulting from any ideas, methods, instructions or products referred to in the content.